Inter-comparison of ABL height estimates from different profiling sensors and models in the framework of HyMeX-SOP1

Donato Summa[1,2], Fabio Madonna[1] , Noemi Franco[2], Benedetto De Rosa[1,2] and Paolo Di Girolamo[2*]

[1]Consiglio Consiglio Nazionale delle Ricerche—Istituto di Metodologie per l'Analisi Ambientale
(CNR-IMAA), 85050, Tito Scalo, Potenza, Italy
[2]Scuola di Ingegneria, Università degli Studi della Basilicata, via Ateneo Lucano 10, 85100 Potenza, Italy

*Correspondence to: Paolo Di Girolamo (paolo.digirolamo@unibas.it)

Abstract. This paper reports results from an inter-comparison effort involving different sensors/techniques used to measure the Atmospheric Boundary Layer (ABL) height. The effort took place in the framework of the first Special Observing Period of the Hydrological cycle of the Mediterranean Experiment (HyMeX-SOP1). Elastic backscatter and rotational Raman signals collected by the Raman lidar system BASIL were used to determine the ABL height and characterize its internal structure. These techniques were compared with co-located measurements from a wind profiler and radiosondes and with ECMWF-ERA5 data. In the effort we consider radiosondes launched in the proximity of the lidar site, as well as radiosondes launched from the closest radiosonde station included in the Integrated Global Radiosonde archive (IGRA). The inter-comparison effort considers data from October 2012. Results reveal a good agreement between the different approaches, with values of the correlation coefficient R^2 in the range 0.52 to 0.94. Results clearly reveals that the combined application of different techniques to distinct sensors' and model datasets allow getting accurate and cross-validated estimates of the ABL height over a variety of weather conditions. Furthermore, correlations between the ABL height and other atmospheric dynamic and thermodynamic variables as CAPE, friction velocity and relative humidity are also assessed to infer possible mutual dependences.

1. Introduction

The ABL is lowest portion of the atmosphere, directly in contact and influence by the Earth's surface , which reacts to the combined action of mechanical and thermal forcing factors. In this layer, as a result of turbulent air motion and vertical mixing induced by shear and buoyancy forces (Stull, 1988), physical quantities such as flow velocity, temperature and moisture are characterized by rapid fluctuations. The variability of these quantities is typically considered to estimate the ABL height.

The evolution of the ABL structure and height has an important impact on meteorology. Accurate measurements of the ABL height (ABLH) allows validating air quality and forecast models and improve specific physical schemes, among others, the boundary layer turbulence and shallow convection parameterizations. However, the complexity of the phenomena occurring within the ABL and the influence of advection and local accumulation processes, in many cases prevents an unambiguous

determination of the ABLH from e.g. the elastic lidar signals, especially when aerosol stratifications are present within the ABL (Haeffelin et al., 2012).

Various methods have been reported in the literature to estimate the ABLH from the vertical profiles of different atmospheric variables. The five most used approaches are: 1) Turbulence method (Stull, 1988), 2) Temperature gradient method (Bianco and Wilczak, 2002, Zeng et al. 2004, Seidel at al. 2012), 3) Richardson number method (Joffre et al., 2001, Sicard et al., 2006), 4) Wind (Melgarejo and Deardorff,1974) and wind shear (Hyun et al., 2005) profile methods, and 5) the combined cloud top and relative humidity method (Lenschow et al., 2000), this latter being applicable only in the presence of stratocumulus-topped boundary layers. A review of these different methodologies was reported by Dai et al. (2014). Some of these approaches are included in the inter-comparison effort illustrated in the present paper.

A convenient, reliable and widely used approach to determine the ABL height and structure both in daytime and night time is based on the identification of local maxima in potential temperature vertical gradient profiles as measured by meteorological radiosondes (Cramer, 1972; Oke, 1988; Stull, 1988; Sorbjan, 1989; Garratt, 1992; Van Pul et al., 1994; De Wekker et al., 1997; Martucci et al.,2007; Behrendt et al., 2011). Specifically, potential temperature tends to keep nearly constant with height within the mixed layer. The level of maximum potential temperature vertical gradient identifies the transition from a convectively unstable region, located below the maximum, to a stable or more stable region, located above the maximum (Summa et al. 2013). Gradient-based methods are accurate and effective in the determination of the ABLH, especially in case of usual ABL conditions and characteristics (Dang et al., 2019), with small computation costs.

In the present paper this approach is applied to radiosounding data from one station included in the IGRA database and results are compared with independent ABLH estimates from co-located elastic backscatter lidar and wind profiler measurements, from ECMWF model reanalysis, as well as from other standard methods applied to radiosoundings data. As a result of recent technological progresses, lidar systems are presently able to provide continuous measurements of atmospheric variables, as particle backscatter or water vapour concentration profiles, and thus allow providing continuous measurements of the ABLH. Wind profilers are quite effective in providing long-term ABLH measurements as a result of their unattended operation over extended observation periods and the availability of an extensive network of operational wind profilers over wide areas of the globe. An effective approach to determine the ABLH from wind profiler signal-to-noise ratio (SNR) measurements was developed by Angevine et al. (1994) in the early nineties. However, the operational use of wind profilers is limited by their lack of sensitivity within the surface atmospheric layer (up to 500 m), which prevents from an adequate monitoring of the ABLH and structure at night or in the presence of shallow ABLs. Additionally, ABLH estimates from wind profilers are very sensitive and frequently affected by the presence of insects' swarms.

In the present research effort we consider Raman lidar measurement from BASIL collected in Southern France in the period September-November 2012 in the frame of HyMeX-SOP1. We focus our attention on the measurements carried out during October 2012. This paper does not represent the first research effort dedicated to an extensive inter-comparison of different ABLH sensors/methodologies. In a previous paper, Seibert et al. (2000) compared different methods to estimate the ABLH

65 from radiosounding data and other instruments and carefully examined advantages and shortcomings of all investigated approaches.

The considered approaches are shortly summarized in what follows. The turbulence method identifies the ABLH as the depth of the lowest continuous turbulence layer (Stull, 1988). The turbulent region is determined by tracking the fluctuations of the different wind components (U, V, and W), for example through a high-pass wavelet filter (Wang et al. 1999). Such

70 fluctuations can be identified in wind lidar data, but measurements can also be performed with radiosondes and tethered balloons or in-situ sensors on-board scientific aircrafts. The ascent velocity of tethered balloons can be carefully controlled to cope with the desired time-height resolution. However, in case of high wind speed or strong convective activity, tethered balloons are inapplicable. A major advantage of the use of aircraft sensors is the simultaneous measurements of both mean and turbulent quantities with high sampling rates. However, lack of observations from the lower atmospheric levels may

75 result from limitations and restrictions to low level flights.

The temperature gradient method relies on the identification of temperature inversions, which are found to typically cap the ABL top and determine a maximum in the potential temperature lapse rate (Bianco and Wilczak, 2002; Martucci et al. 2007). Potential temperature $\theta(z)$, which is a function of atmospheric pressure and temperature, is given by the expression:

$$\theta(z) = T(z) \left(\frac{P_0}{P(z)}\right)^{\frac{R}{Cp}} \tag{1}$$

80 with P_0 is the standard pressure, T and P are the pressure and temperature, respectively, at altitude z, with is $R/Cp = 0.286$.
$\theta(z)$ tends to keep nearly constant with height within the mixed layer. The level of the maximum vertical gradient in potential temperature indicates the transition from a convectively unstable region, located below this maximum, to a stable or more stable region, located above the maximum. The stable layer at the top of the mixed layer stops the turbulent eddies from further rising. Stable layers characterized by increasing temperatures with height (positive lapse rates, called capping

85 inversions) can prevent the development of deep convection. During the day, the level at which air parcels become negatively buoyant corresponds to a main temperature inversion. Such inversions can be identified in radiosonding data, with radiosondes providing very accurate information throughout the troposphere. Additionally, radiosonding data can provide a long observational record, which is particularly suited for ABLH climatological studies (Madonna et al. 2021). However, radiosonde measurements are characterized by lack of temporal resolution (only 2–4 launches per day from each station) and

90 a poor geographical distribution, with an uneven distribution density in the two hemispheres.

The Richardson number method relies on the identification of Richardson number gradients, which is an important diagnostic indicator of dynamic flow stability. This method assumes the ABLH to be the level where the so called "bulk Richardson number for the entire ABL" exceeds a specific threshold value, Ri_{bc}. Ri_{bc} at height z can be calculated from the wind speed and the potential temperature values at z and at surface level, as originally reported in Hanna (1969) and

95 extensively described in e.g., Stull (1988) and Garratt (1994). Such gradients can be revealed in wind lidar, wind profiler, radiosonde and aircraft in- situ sensors' profile data (Sicard et al., 2006).

The ABLH can also be estimated from the vertical wind profile, using e.g. the lowest wind-speed maximum height, often referred to as the low-level jet (LLJ) height (Melgarejo and Deardorff,1974). The LLJ height is again identifiable in wind lidar, wind profiler, radiosonde and aircraft in-situ sensors' profile data.

100 The paper outline is the following. Section 2 shortly describes the profiling sensors and model data involved in the inter-comparison effort. Section 3 illustrates the results from the inter-comparison effort. Finally, section 4 provides a summary, concluding remarks and indications for possible future follow-on studies.

2 Profiling sensors and model data involved in the inter-comparison effort

105

2.1 BASIL System

The University of BASILicata ground-based Raman Lidar system (BASIL) was deployed in the Cévennes-Vivarais (CV) site (Candillargues, Southern France, Lat: 43°37' N, Long: 4° 4' E, Elev: 1 m, figure 1) and operated between 5 September
110 and 5 November 2012, collecting more than 600 hours of measurements, distributed over 51 measurement days and 19 intensive observation periods (IOPs, Di Girolamo *et al.*, 2016; Stelitano *et al.*, 2019). BASIL is capable to perform high-resolution and accurate measurements of atmospheric temperature and water vapour, both in daytime and night-time, based on the application of the rotational and vibrational Raman lidar techniques, respectively, in the UV (Di Girolamo *et al.*, 2004, 2009, 2017). This measurement capability makes BASIL an effective tool for the characterization of water vapour
115 inflows in Southern France, which are a key ingredient of heavy precipitation events in the North-western Mediterranean basin. BASIL makes use of a Nd:YAG laser source capable of emitting pulses at 355, 532 and 1064 nm, with single pulse energies at 355 nm, i.e. the wavelength used to stimulate rotational and roto-vibrational Raman scattering from atmospheric molecules, of 500 mJ (average optical power of 10 W at a laser repetition rate of 20 Hz). The receiver includes a Newtonian telescope in (45-cm diameter primary mirror). Data are acquired with a rough vertical and temporal resolution of 30 m and
120 10 sec, respectively, but vertical and temporal smoothing is typically applied when processing water vapour and temperature profile measurements for data assimilation purposes or process studies.

2.2 Determination of the ABLH from Raman lidar measurements

There are several methodologies to determine the ABL height from elastic lidar signals, which rely on the circumstance that
125 aerosols are more abundant within the ABL than in the free troposphere and they can act as tracers of atmospheric motions. An extensively used methodology relies on the detection of vertical gradients in elastic backscatter lidar echoes, which result from such echoes being much stronger within the ABL than in the free troposphere.

The elastic lidar equation, expressed in terms of number of collected photons as function of height, is defined as:

$$P_{\lambda_0}(z) = P_{\lambda_0} O(z) \frac{A}{z^2} \left[\beta_{par}(z) + \beta_{mol}(z) \right] T_{mol}^2(z) \, T_{par}^2(z) + P_{bgd}(z) \qquad (1)$$

4

Atmospheric
Measurement
Techniques
Discussions

Open Access

EGU

130   where λ_0 is the emitted and received lidar wavelength, respectively, z is the vertical height, P_{λ_0} is the number of laser emitted

photons, $O(z)$ is the overlap function, A is the telescope collection area, $\beta_{mol}(z)$ and $\beta_{par}(z)$ is the backscatter coefficient for

molecules and particles, respectively, $T_{mol}(z)$ and $T_{par}(z)$ represent the molecular and particle contribution to atmospheric

transmissivity, respectively, and P_{bgd} is the background signal associated with solar irradiance and detectors' noise. In order

to compress the signal dynamical variability and define an uncalibrated quantity proportional to total (molecular + particle)

135   attenuated backscattering coefficient, it is often preferable to make use of the range-corrected signals (RCSs), which is

defined as:

$$P_{RCS}(z) = \left[P_{\lambda_0}(z) - P_{bgd}(z)\right]z^2 \tag{2}$$

The ABL height is estimated from the height derivative of RCSs through the expression:

$$ABLH = min\left\{\frac{d}{dz}\left[\log\left(P_{RCS}(z)\right)\right]\right\} \tag{3}$$

140   Transitions between different aerosol layers are identified with the minima in expression (3), with the absolute minimum

typically representing the ABLH. For the specific purposes of our present study, the elastic backscatter signal at 355 nm,

$P_{355}(z)$, is considered in expression (2). The methodology is applied to signals with vertical and time resolutions of 30 m and

5 min, respectively (Summa at al ., 2013; Vivone et al., 2021). Overlap effects affect lidar signals in the lower few hundred

meters have marginal effects on gradient measurements and consequently ABLH estimates.

145

2.3 WIND profiler

The five-beam wind profiler (WPR) considered in the study was also deployed in Candillargues. The system is manufactured

by Degreane (model PCL 1300) and operates in the UHF band with a primary frequency at 1.274 GHz.. A detailed

150   description of the WPR, its specifications and main working parameters, data processing methodologies and delivered

geophysical products are illustrated in Saïd et al. (2016). The WPR operated almost continuously throughout the duration of

HyMeX-SOP1 (Saïd et al., 2018). For the ABL height measurements reported in this paper, the WPR was operated in low

mode, with a pulse length of 1μs. This allows sampling the lower troposphere from 0.15 to 5.7 km a.g.l., with a vertical

resolution of 150m. The methodology to determine the ABL height relies on the identification of a distinctive strong peak in

155   the WPR time-height reflectivity plot (Gage et al., 1990), though the strength of this peak may depend on a variety of

factors. While this approach is very effective in the determination of the ABLH, its applicability can be limited by the

presence of strong reflectivity peaks associated with marked temperature and humidity gradients. This is the primary

uncertainty source WPR-based ABLH measurements. This aspect will be carefully accounted for when comparing the

different approaches.

160

2.4 Radiosoundings

A radiosonde launching facility was setup in Candillargues in September 2012 for the purposes of HyMeX-SOP1. Launched

radiosondes, manufactured by Vaisala (model: RS92), were launched without a predefined schedule, primarily during the

165   intensive observation periods, with a launching rate of up to one launch every 1.5 h. The radiosondes were set to provide vertical profiles of atmospheric pressure, temperature, humidity, and wind direction and speed during both the ascent and descent phases. The thin-wire temperature sensor, whose measurements are used for the ABLH estimate, is characterized by a very fast response time and has a hydrophobic coating protection to reduce the effects of evaporative cooling after emerging from clouds (Dirsken et al., 2014; Madonna et al., 2020). ABLH estimates are obtained from the radiosonde data based on the application of the temperature gradient method, which relies on the identification of maxima in the potential

170   temperature vertical gradient. Small, but non-negligible uncertainties (0.05 K) may affect radiosonde temperature measurements as a result of the sonde's pendulum motion and the resulting increased sensor ventilation (Dirksen al., 2014), with again marginal effects on temperature gradient measurements and consequently ABLH estimates.

2.5 IGRA DataBase

175   ABLH estimates from BASIL and WPR measurements carried out during HyMeX-SOP1 were compared with those obtained from the radiosondes launched from nearest Integrated Global Radiosonde archive (IGRA) radiosounding station. IGRA is the most comprehensive, authoritative collection of historical and near-real-time radiosonde and pilot balloon observations, with global coverage, maintained and distributed by the National Oceanic and Atmospheric Administration's National Centers for Environmental Information (NCEI). Data are extracted from version V2 IGRA database, which was

180   released in 2016 (Durré et al., 2018) and includes enhanced quality with respect to the previous version (V1). ABLH estimates from IGRA radiosondes are obtained based using agin the temperature gradient method. The specific IGRA station considered in our study is Nimes-Courbessac (lat: 43.8569°N, 4.4064°E, 60 m asl, WMO index= 7645), typically carrying out four radiosonde launches per day and using GPS radiosondes manufactured by Meteomodem (model: M10). The performance of M10 radiosondes was assessed and verified to be accurate during the WMO 2010 radiosonde inter-

185   comparison effort in Yangjang (Nash et al., 2011, Madonna et al. 2021), being again characterized by negligible uncertainties in temperature gradient measurements and consequently ABLH estimates.

2.6 ECMWF-ERA5

ABLH estimates from the aforementioned observational sources have been also compared with ECMWF-ERA5 atmospheric

190   reanalysis. ECMWF-ERA5 is the latest reanalysis produced by ECMWF, including hourly data on a regular latitude-longitude grids, with a 0.25° x 0.25° resolution (Hersbach et al., 2020) and atmospheric parameters provided at 2m and at an additional 36 pressure levels. ERA5 is publicly available through the Copernicus Climate Data Store (CDS, https://cds.climate.copernicus.eu).

In order to properly carry out the comparison, the nearest ERA5 grid point to the CV site was considered, assuming the

195   representativeness uncertainty associated with the use of the nearest grid-point to be comparable with the uncertainty affecting most interpolation approaches (e.g. kriging, bilinear interpolation, etc.). In general, reanalysis reliability can considerably vary depending on the location, time and selected atmospheric variable (Dee et al., 2016). Mixed layer

parametrizations in atmospheric forecast models typically consider boundary layer height estimates from entraining parcel models. However, to guarantee an effective and reliable ABLH monitoring, also in neutral and statically stable atmospheric

200 conditions, the bulk Richardson number method is frequently preferred as an independent diagnostic proxy in turbulence parametrization (Seidel et al., 2012), this also being the method considered in the present paper. The algorithm used in ERA5 requires approximations, which ultimately increase uncertainties (Seidel et al., 2012): for example, the lack of accurate information on the local surface roughness affects friction velocity estimates and, consequently, surface frictional effects are ignored in the computation of the bulk shear.

205 The ERA5 ABLH is defined as the lowest level at which the bulk Richardson number reaches the critical value of 0.25 in both convective and stable boundary layers. In ECMWF Integrated Forecasting System (IFS) the bulk Richardson number is computed as follows:

$$Ri_b = h_{bl} \frac{2g(s_{vhbl}-s_{vn})}{(s_{vhbl}+s_{vn}-gh_{bl}-gz_n)|\Delta U|^2} \tag{4}$$

where The index n identifies the lowest model level and the index hbl identifies the boundary layer height, i.e the level here

210 the bulk Richardson number reaches the critical value of 0.25. The virtual dry static energy from the lowest level:

$$s_{vn} = c_p T_n (1 + \varepsilon q_n) + gz_n \tag{5}$$

is compared to the virtual dry static energy at the boundary layer top:

$$s_{vhbl} = c_p T_{hbl} (1 + \varepsilon q_n) + gz_n \tag{6}$$

and

215
$$|\Delta U|^2 = u^2{}_{hbl} + v^2{}_{hbl} \tag{7}$$

$u^2{}_{hbl}$ and $v^2{}_{hbl}$ being the are the horizontal wind speed components at the ABLH. The ABLH is obtained from both the radiosonde and model data using this algorithm, which is applied from the surface upwards. In case the ABLH falls in between two levels, a linear interpolation is applied to determine its exact position.

In the present paper we provide ABLH estimates based on the application of different approaches with the aim to assess the

220 performance achievable with each observational or model data and verify their applicability in different atmospheric scenarios. In the attempt to ensure the highest possible performance achievable with each observational or model data, deviations observed the in the comparison of the different datasets sensors and mothers and approaches are carefully analyzed and discussed, also counting for results from previous inter-comparison efforts (Seidel et al., 2012).

225 **3. Results**

In this section we illustrate and discuss the ABLH estimates as obtained from measurements/model data through the application of the five different approaches/sensors/models illustrated in the previous sections. We first provide a more climatological assessment, focusing on the evolution of the ABLH throughout the duration of the month of October 2012. Figure 2 illustrates the time evolution of the ABLH as measured/modeled through these approaches. ABLH lidar estimates

230 illustrated and discussed in this paper were obtained from the Raman lidar measurements collected during the period 1-31

October 2012 by BASIL (Figure 1). Specifically, figure 2a illustrates the mean values obtained by averaging ABLH estimates throughout the duration of the day over the time window from 9:00 to 21:00 UTC. This time interval includes information from the entire daytime portion of the day, thus allowing to account for the complete duration of the daily convective activity, from it activation in the morning to its decay in the evening. The results in the figure 2a reveal a quite

235 good agreement between the five different approaches/sensors/models, all of the them being capable to capture the major features associated with ABLH monthly variability, with the only exception of ERA5 model reanalyses which underestimate the ALBH over an extended portion of the considered period (16-31 October 2012). A definitive and unambiguous motivation for these lower ABLH values was not identified. A reasonable hypothesis is that the size of the ERA5 model grid point is large enough (30 km × 30 km) to limit representativeness of the reanalysis results when compared to point

240 measurements. In this regard, it is to be specified that the CV measurement site is located few hundred meters inland and the ERA5 grid point includes both land and sea areas. Additionally, the second half of the month of August 2012 was characterized by a much larger variability of weather conditions and lower horizontal homogeneity of most atmospheric variables.

Figures 2b and 2c illustrate the deviations, expressed both in meters and in percentage (%), between the ABLH estimated

245 from the 5 different approaches/sensors/models considered and the mean value of the 5, this latter value being considered as reference. These values are also reported in table 1. With the only exception of few data points, deviations are always within ± 200 m and ± 20 %. The mean value of the bias of each sensor with respect to the reference value has also been computed. The largest deviations are again observed between ERA5 model and all other sensors during the second half of the month, with a negative bias in ERA5 data in the range 11-42 % and about 200-800 m. For the radiosondes in Candillargues, the

250 IGRA radiosondes, the wind profiler, BASIL and ERA5, the mean bias with respect to the mean ABLH estimate are 77.0 m (4.6 %), 44.2 m (4.5 %), 38.1 m (1.87 %), -9.6 m (-0.09 %)and -149.7 m (-10.8 %), respectively. Because of the large bias affecting ERA5 data from the second half of the month of October 2012, ERA5 data were removed from the computation of the mean reference ABLH in the forthcoming regression analysis. Additionally, when ERA5 data from the second half of the month of October 2012 are removed from the mean reference ABLH estimate, the mean bias of the radiosondes in

255 Candillargues, the IGRA radiosondes, the wind profiler, BASIL and ERA5 with respect to the mean ABLH estimate are 47.9 m (2.5 %), 15.1 m (2.3 %), 9.0 m (0.2 %), -38.7 m (-2.1 %)and -178.8 m (-12.1 %), respectively.

Figure 3 compares ABLH estimates obtained from the different sensor/model data in terms of scatter plot. A linear fit is applied to the data points, using a linear regression function through zero with the form $Y = A \times X$, with X being again the values of the mean reference ABLH obtained from the 5 different sensors/models and Y being ABLH values from each

260 single sensor/model. The slope of the regression line, i.e. the term A, provides an alternative estimate of the bias of each sensor/model. The correlation coefficient R^2 quantifies the degree of agreement between the values of the compared sensors/models. Values of A and R^2 for each sensor/model are reported in the table 1. All values of R^2 are in the range 0.81-0.94 (with the only exception of the ERA5, with $R^2=0.52$), which testifies a good level of agreement between the different approaches/sensors/models. Specifically, figure 3a compares ABLH values from the radiosondes in Candillargues with the

265   reference ABLH values, with R^2 being equal to 0.94 and A being equal to 1.04, which confirms a small positive bias (4 %)
affecting these radiosondes when compared with the reference estimate. Figure 3b compares ABLH values from the IGRA
radiosondes with the reference ABLH values, with R^2 being equal to 0.81 and A being equal to 1.00, which confirms the
very good agreement between these radiosondes and all other sensors/models. Figure 3c compares ABLH values from the
wind profiler with the reference ABLH values, with R^2 being equal to 0.93 and A being equal to 1.01, which confirms a very

270   small positive bias (1 %) affecting the wind profiler when compared with the reference estimate. Figure 3d compares ABLH
values from BASIL with the reference ABLH values, with R^2 being equal to 0.91 and A being equal to 0.97, which confirms
a very small negative bias (3 %) affecting BASIL when compared with the reference estimate. Finally, 3e compares ABLH
values from ERA5 with the reference ABLH values, with R^2 being equal to 0.52 and A being equal to 0.87, which confirms
the limited level of correlation of ERA5 data with the other sensors and the large negative bias (13 %) affecting these data

275   when compared with the reference estimate. The regression analysis results are summarized in table 2.
Additional parameters from ERA5 reanalysis data have been considered to corroborate the analysis the data and the
interpretation of the observed atmospheric features. Figure 4 shows the time evolution of the Convective Available Potential
Energy (CAPE, panel a) and the friction velocity (panel b) from ERA5 reanalysis and relative humidity over the time period
1-31 October 2012. Friction velocity quantifies the vertical transport of momentum, or turbulence generation. It is calculated

280   as the square root of the surface stress divided by air density. Friction velocity includes both a turbulent and a viscous
component. In a turbulent flow, friction velocity is approximately constant within the few lowest meters of the atmosphere.
This parameter increases with surface roughness. CAPE quantifies atmospheric instability, with large positive values (>400)
being necessary for the onset of convective activity in a conditionally unstable tropospheric layer. Peak values in friction
velocity are found in association with the highest ABLH daily mean values. During the month of October 2012 this happens

285   around 18-19 October. This result confirms the important role played by the vertical transport of momentum and turbulence
in the development of the ABL and in ABLH growth. CAPE values on 18-19 October 2012 are in the range 50-10 J kg^{-1},
which are indicative of high stability conditions of an atmospheric environment un favorable to convective activity on these
days.
We also compared and tried to quantitative correlate ABLH estimates with the variability of specific atmospheric dynamic

290   and thermodynamic variables, as CAPE, friction velocity and relative humidity. CAPE daily gradient values were computed
considering the time series of CAPE values during the time interval 1-31 October 2012. A linear fit was applied to the time
series of CAPE daily gradient and the friction velocity values in the time period 1-31 October 2012 vs. the corresponding
ABLH estimates. Considered ABLH estimates are those from ERA5 reanalysis and the mean of the 5 different
approaches/sensors/models considered above. The correlation between ERA5 ABLH estimates and the corresponding

295   friction velocity values is found to be 0.71, while the correlation between the mean ABLH estimates and the ERA5 friction
velocity values is found to be 0.75. The correlation between ERA5 ABLH estimates and the corresponding CAPE daily
gradient values is 0.49, while the correlation between the mean ABLH estimates and the ERA5 CAPE daily gradient values
is found to be 0.52. Finally, the correlation between ERA5 ABLH estimates and the corresponding relative humidity values

is 0.32, while the correlation between the mean ABLH estimates and the ERA5 relative humidity values is 0.42. These

300 values reveal a good correlation between ABLH estimates and corresponding friction velocity values, a very mild correlation between ABLH estimates and corresponding CAPE daily gradient values and a missing correlation between ABLH estimates and corresponding relative values. These results are summarized in table 3.

For the purpose of assessing the performance in the characterization of the short-term variability, our analysis was also focused on one specific case study, covering the daytime portion of 18 October 2012. Figure 5a illustrates the time-height

305 cross-section of the particle backscattering coefficient at 355nm, $\beta_{355}(z)$, as measured by BASIL measurements of over the time interval 09:26-21:11 UTC on 18 October 2012. The map is conceived as a succession of consecutive $\beta_{355}(z)$ profiles, each one with an integration time of 5 min and a vertical resolution of 150 m. Red dots in the figure identify the ABLH values obtained through the application of the approach illustrated in the section 2.2 to BASIL measurements. The yellow stars identify the ABLH values determined through the application of the temperature gradient method to the radiosonde

310 data. During the measurement session the ABLH is found to vary from an initial value of ~1.5 km around 09:30 UTC to a maximum value of ~2.3 km around 19:40 UTC, descending down to ~1.7 km around 21:15 UTC. On this day an elevated Mesoscale Convective System (MCS) is found to transit over the lidar station, with the cloud system base ranging between 2.5 and 4.5 km. Light precipitations are observed around 11 and 12 UTC, while virga events, with precipitating particles sublimating before reaching the ground, are observed later in the afternoon in the time interval 17-19 UTC. Figure 5a also

315 includes ABLH estimates obtained from the application of the temperature gradient method to the the IGRA radiosounding data (blue star), these values being in very good agreement with those simultaneously estimated from the lidar data.

Figure 5b illustrates the time-height cross-section of the water vapour mixing ratio measurements carried out by BASIL on the same day, which are displayed over the same time intervals considered in figure 5a. A dry layer appears at the ABL top, probably resulting from sub-cloud low-level rain evaporation. This dry layer may ultimately have contributed to convection

320 regeneration events observed throughout the passage of the MCS (Li et al. 2009; Morrison et al. 2009). It is to be specified that rain evaporation significantly contributes to the heat and moisture budgets of clouds (Emanuel et al., 1994), but few observations of these processes are available (Gamache et al., 1993). Dry layers are frequently observed in mid-latitude convective environments as a result of air being advected from different source regions under directionally sheared vertical wind profiles (Carlson and Ludlam 1968). Deep convective precipitation events are influenced, and frequently favored, by

325 the presence of aerosols and midlevel dry layers, and this circumstance may have played a significant role in the formation and development of the observed MCS.

4. Conclusions

In the present paper we illustrate and discuss the results from an inter-comparison effort considering ABL height estimates

330 from different sensors/techniques. The effort was carried out in the framework of HyMeX-SOP1. A climatological assessment focusing on the evolution of the ABL height throughout the duration of the month of October 2012 is provided. Results reveal a good agreement between the different sensors/approaches, all of the them being able to capture the major

ABL height features, with the exception of ERA5 reanalysis which underestimates the ABL height over an extended portion of the considered period (16-27 October 2012). The R^2 computed form different sensor are in the range 0.81-0.94, with the

335 only exception of the value for ERA5 (0.52). The biases of the single sensors/models with respect to the mean value of the five, this latter value being considered as a reference, was also estimated. These biases were estimated through both a simple statistical analysis (mean deviation between the single sensors/model values and the reference values) and a regression analysis (slope of the linear fit regression line correlating the single sensor/model values and the reference values), with all bias values being smaller than 4 %, with the only exception of ALBH estimated from ERA5 model reanalyses which

340 underestimate the reference ALBH values by 12-13 %. The analysis was integrated with the consideration of a variety of atmospheric dynamic and thermodynamic variables from ERA 5, with friction velocity found to be one of the main drivers of ABL variability. The analysis was also focused on one specific case study, covering the daytime portion of 18 October 2012, for the purpose of assessing the performance in the characterization of the short-term variability,.

345 **5. Acknowledgments**

References

Angevine, W.M., White, A.B. & Avery, S.K. Boundary-layer depth and entrainment zone characterization with a boundary-layer profiler. Boundary-Layer Meteorol 68, 375–385 (1994). https://doi.org/10.1007/BF00706797.

355 Behrendt, A., Pal, S., Aoshima, F., Bender, M., Blyth, A., Corsmeier, U., Cuesta, J., Dick, G., Dorninger, M., Flamant, C., Di Girolamo, P., Gorgas, T., Huang, Y., Kalthoff, N., Khodayar, S., Mannstein, H., and Wulfmeyer, V.: Observation of Convection Initiation Processes with a Suite of State-of-the-Art Research Instruments during COPS IOP8b, Q. J. Roy. Meteorol. Soc., 137, 81–100, doi:10.1002/qj.758, 2011.

Bianco, L., and Wilczak, J. M. (2002) Convective boundary layer depth: improved measurement by Doppler radar wind

360 profiler using fuzzy logic methods. J Atmos Oceanic Technol 19:1745–1758.

Carlson, T.N. and Ludlam, F.H. (1968), Conditions for the occurrence of severe local storms. Tellus, 20: 203-226. https://doi.org/10.1111/j.2153-3490.1968.tb00364.x.

Cramer, O. P.: Potential temperature analysis for mountainous terrain, J. Appl. Meteor., 11, 44–50, 1972.

Dai H., K Katherine, L. Milkman Jason Riis The Fresh Start Effect: Temporal Landmarks Motivate Aspirational Behavior

365 October 2014, DOI: 10.1287/mnsc.2014.1901.

Dang, R.; Yang, Y.; Li, H.; Hu, X.-M.; Wang, Z.; Huang, Z.; Zhou, T.; Zhang, T. Atmosphere Boundary Layer Height (ABLH) Determination under Multiple-Layer Conditions Using Micro-Pulse Lidar. Remote Sens. 2019, 11, 263. https://doi.org/10.3390/rs11030263.

Dee, D. P., , J. Fasullo, , D. Shea, , J. Walsh, and N. S., Eds., 2016: The climate data guide: Atmospheric reanalysis: Overview and comparison tables. [Available online at https://climatedataguide.ucar.edu/climate-data/atmospheric-reanalysis-overview-comparison-tables.]

De Wekker, S. F. J., Kossmann, M., and Fielder, F.: Observations of daytime mixed layer heights over mountainous terrain during the TRACT field campaign. Proc. 12th Symp. on Boundary Layers and Turbulence, Vancouver, BC, Canada, Am. Meteor. Soc., 1, 498–499, 1997.

Di Girolamo, P., R. Marchese, D. N. Whiteman, B. B. Demoz, Rotational Raman Lidar measurements of atmospheric temperature in the UV. Geophysical Research Letters, 31, L01106, ISSN: 0094-8276, doi: 10.1029/2003GL018342, 2004.

Di Girolamo, P., D. Summa, R. Ferretti, Multiparameter Raman Lidar Measurements for the Characterization of a Dry Stratospheric Intrusion Event. Journal of Atmospheric and Oceanic Technology, vol. 26, p. 1742-1762, ISSN: 0739-0572, doi: 10.1175/2009JTECHA1253.1, 2009.

Di Girolamo, P., C. Flamant, M. Cacciani, E. Richard, V. Ducrocq, D. Summa, D. Stelitano, N. Fourrié and F. Saïd, Observation of low-level wind reversals in the Gulf of Lion area and their impact on the water vapour variability, Quarterly Journal of the Royal Meteorological Society, 142 (Suppl 1): 153–172, doi: 10.1002/qj.2767, 2016.

Di Girolamo, P., M. Cacciani, D. Summa, A. Scoccione, B. De Rosa, A. Behrendt, V. Wulfmeyer (2017), Characterisation of Boundary Layer Turbulent Processes by the Raman Lidar BASIL in the frame of HD(CP)2 Observational Prototype Experiment, Atmospheric Chemistry and Physics, 17, 745-767, doi:10.5194/acp-17-745-2017.

Dirksen, R. J., Sommer, M., Immler, F. J., Hurst, D. F., Kivi, R., and Vömel, H.: Reference quality upper-air measurements: GRUAN data processing for the Vaisala RS92 radiosonde, Atmos. Meas. Tech., 7, 4463–4490, https://doi.org/10.5194/amt-7-4463-2014, 2014.

Durre, I., Yin, X., Vose, R. S., Applequist, S., & Arnfield, J. (2018). Enhancing the Data Coverage in the Integrated Global Radiosonde Archive, Journal of Atmospheric and Oceanic Technology, 35(9), 1753-1770.

Emanuel, K. A., Neelin, J. D. & Bretherton, C. S. On large-scale circulations in convecting atmospheres. Q. J. R. Meteorol. Soc. 120, 1111–1143 (1994).

Gage, K. S., B. B. Balsley, W. L. Ecklund, R. F. Woodman, and S. K. Avery, Wind-profiling Doppler radars for tropical atmosphericresearch, Eos Trans. AGU, 71, 1851–1854, 1990.

Gamache, J. F., Houze, R. A. & Marks, F. D. Dual-aircraft investigation of the inner core of hurricane Norbert. 3. Water-budget. J. Atmos. Sci. 50, 3221–3243 (1993).

Garratt, J. R.: The Atmospheric Boundary Layer, Cambridge Atmospheric and Space Science Series, Cambridge Univ. Press, 335 pp., 1992

400   Garratt, J. Review: The atmospheric boundary layer. Earth Sci. Rev. 1994, 37, 89–134.

Hanna, Steven R., The thickness of the planetary boundary layer, Atmospheric Environment (1967), Volume 3, Issue 5, 1969, Pages 519-536, ISSN 0004-6981, https://doi.org/10.1016/0004-6981(69)90042-0.

Haeffelin, M., Angelini, F., Morille, Y., Martucci, G., O'Dowd, C. D., Xueref-Rémy, I.,Wastine, B., Frey, S., and Sauvage, L.: Evaluation of mixing depth retrievals from automatic profiling lidars and ceilometers inview of future integrated

405   networks in Europe, Bound.-Lay. Meteorol., 143, 49–75, doi:10.1007/s10546-011-9643-z, 2012.

Hersbach et al.: The ERA5 reanalysis, Quarterly Journal of Royal Meteorology Society, 17 May 2020, accepted, https://doi.org/10.1002/qj.3803.

Hyun Y, Kim K-E, Ha K-J (2005) A comparison of methods to estimate the height of stable boundary layer over a temperate grassland. Agric For Meteorol 132:132–142

410   Joffre SM, Kangas M, Heikinheimo M, Kitaigorodskii SA (2001) Variability of the stable and unstable atmospheric boundary-layer height and its scales over a boreal forest. Boundary-Layer Meteorol 99:429–450.

Lenschow DH, Zhou M, Zeng X, Chen L, Xu X (2000) Measurements of fine-scale structure at the top ofmarine stratocumulus. Boundary-Layer Meteorol 97:331–357.

Li, J., B.E. Carlson, and A.A. Lacis, 2009: A study on the temporal and spatial variability of absorbing aerosols using total

415   ozone mapping spectrometer and ozone monitoring instrument aerosol index data. J. Geophys. Res., 114, D09213, doi:10.1029/2008JD011278.

Madonna, F., D. Summa, P. Di Girolamo, F. Marra ,Y. Wang and M., Rosoldi, Assessment of Trends and Uncertainties in the Atmospheric Boundary Layer Height Estimated Using Radiosounding Observations over Europe *Atmosphere* 2021, *12*(3), 301; https://doi.org/10.3390/atmos12030301.

420   Madonna, F., Kivi, R., Dupont, J.-C., Ingleby, B., Fujiwara, M., Romanens, G., Hernandez, M., Calbet, X., Rosoldi, M., Giunta, A., Karppinen, T., Iwabuchi, M., Hoshino, S., von Rohden, C., and Thorne, P. W.: Use of automatic radiosonde launchers to measure temperature and humidity profiles from the GRUAN perspective, Atmos. Meas. Tech., 13, 3621–3649, https://doi.org/10.5194/amt-13-3621-2020, 2020.

Martucci G, Matthey R, Mitev V (2007) Comparison between backscatter lidar and radiosonde measurements of the diurnal

425   and nocturnal stratification in the lower troposphere. J AtmosOceanic Technol 24:1231–1244.

Melgarejo J. W., Deardorff JW (1974) Stability functions for the boundary layer resistance laws based upon observed boundary-layer heights. J Atmos Sci 31:1324–1333.

Morrison, H. G., G. Thompson, and V. Tatarskii, 2009: Impact of cloud microphysics on the development of trailing stratiform precipitation in a simulated squall line: Comparison of one and two-moment schemes. Mon. Wea. Rev., 137,

430   991–1007, doi:10.1175/2008MWR2556.1

Nash, J., T. Oakley, H. Vömel, LI Wei: WMO intercomparison of high quality radiosonde systems, WMO/TD-No. 1580, Yangjiang, China, 12 July – 3 August 2010.

Oke, T. R.: Boundary Layer Climates, 2nd Edn., 435 pp., Halsted Press, New York, 1988.

Saïd, F., Campistron, B., Delbarre, H., Canut, G., Doerenbecher,A., Durand, P., Fourrié, N., Lambert, D., and Legain, D.:

435   Offshorewinds obtained from a network of wind-profiler radars duringHyMeX: 3D Wind Fields during HyMeX, Q. J. Roy. Meteor.Soc., 142, 23–42, https://doi.org/10.1002/qj.2749, 2016.

Saïd, F., B. Campistron, and P. Di Girolamo, High-resolution humidity profiles retrieved from wind profiler radar measurements, Atmospheric Measurement Techniques, VOL. 11, Issue 3, 1669-1688, https://doi.org/10.5194/amt-11-

440   1669-2018, 2018.

P. Seibert, F. Beyrich, S.-E. Gryning, S. Joffre, A. Rasmussen, P. Tercier, Review and intercomparison of operational methods for the determination of the mixing height, Atmospheric Environment, Volume 34, Issue 7, Pages 1001-1027, ISSN 1352-2310, https://doi.org/10.1016/S1352-2310(99)00349-0, 2000.

Seidel, D. J., Y. Zhang, A. Beljaars, J.-C. Golaz, A. R. Jacobson, and B. Medeiros, Climatology of the planetary boundary

445   layer over the continental United States and Europe, Journal of Geophysical Research, Vol. 117, D17106, doi:10.1029/2012JD018143, 2012, 2012.

Sicard, M., Pérez, C., Rocadenbosch, F., Baldasano, J.M., García-Vizcaino, D. (2006) Mixed-layer depth determination in the Barcelona coastal area from regular lidar measurements: methods, results and limitations. Boundary-Layer Meteorol 119:135–157.

450   Sorbjan, Z., Structure of the Atmospheric Boundary Layer, New Jersey, Prentice-Hall, 316 p., 1989.

Stelitano, D., P. Di Girolamo, A. Scoccione, D. Summa, and M. Cacciani, Characterization of atmospheric aerosol optical properties based on the combined use of a ground-based Raman lidar and an airborne optical particle counter in the framework of the Hydrological Cycle in the Mediterranean Experiment – Special Observation Period 1, Atmospheric Measurement Techniques, Vol. 12, 2183–2199, doi: 10.5194/amt-12-2183-2019, 2019.

455   Stull, R. B.: An Introduction to Boundary Layer Meteorology, Dordrecht, Kluwer, 666 pp., 1998.

Summa, D., P. Di Girolamo, D. Stelitano, and M. Cacciani, Characterization of the planetary boundary layer height and structure by Raman lidar: comparison of different approaches, Atmos. Meas. Tech., 6, 3515–3525, 2013, www.atmos-meas-tech.net/6/3515/2013/doi:10.5194/amt-6-3515-2013.

Van Pul, W. A., J., Holtslag, A. A. M., and Swart, D. P. J.: A comparison of ABL heights inferred routinely from lidar and

460   radiosondes at noontime, Bound.-Lay. Meteorol., 68, 173–191, 1994.

Vivone, G., G. D'Amico, D. Summa, S. Lolli, A. Amodeo, D. Bortoli, and G. Pappalardo. Atmospheric boundary layer height estimation from aerosol lidar: a new approach based on morphological image processing techniques Atmos. Chem. Phys., 21, 4249–4265, 2021 https://doi.org/10.5194/acp-21-4249-2021.

Wang Q, Lenschow DH, Pan L, Schillawski RD, Kok GL, Prévot ASH, Laursen K, Russell LM, Bandy AR, Thornton DC,

465   Suhre K (1999) Characteristics of the marine boundary layers during two Lagrangian measurements periods Turbolence structure J Geophys Res 104(D17):21767–21784.

Atmospheric
Measurement
Techniques
Discussions
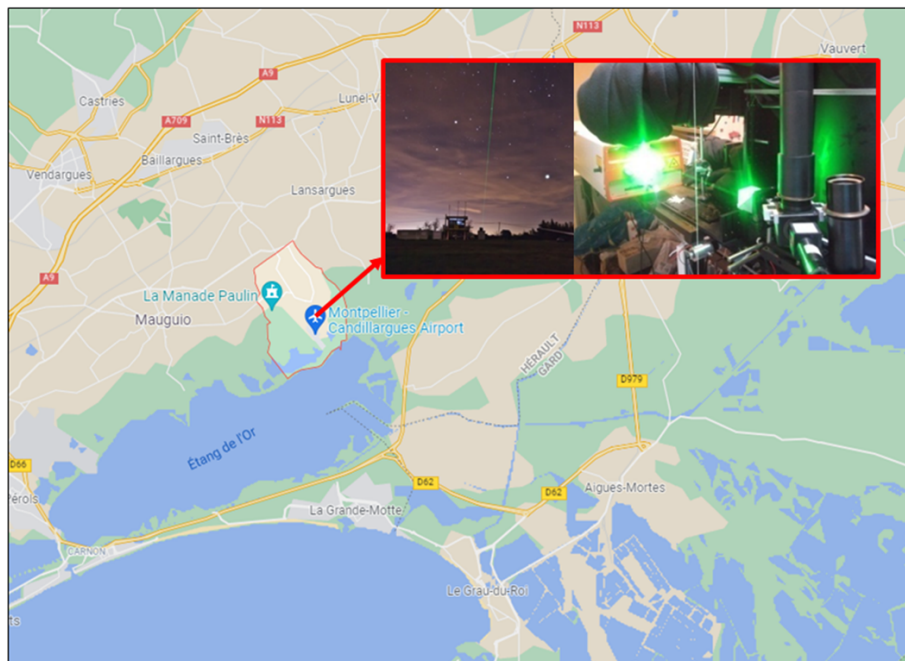
Figure 1: Location and two images of the Raman lidar system BASIL operated during HyMex-SOP1 (© Google Maps
470   2021).
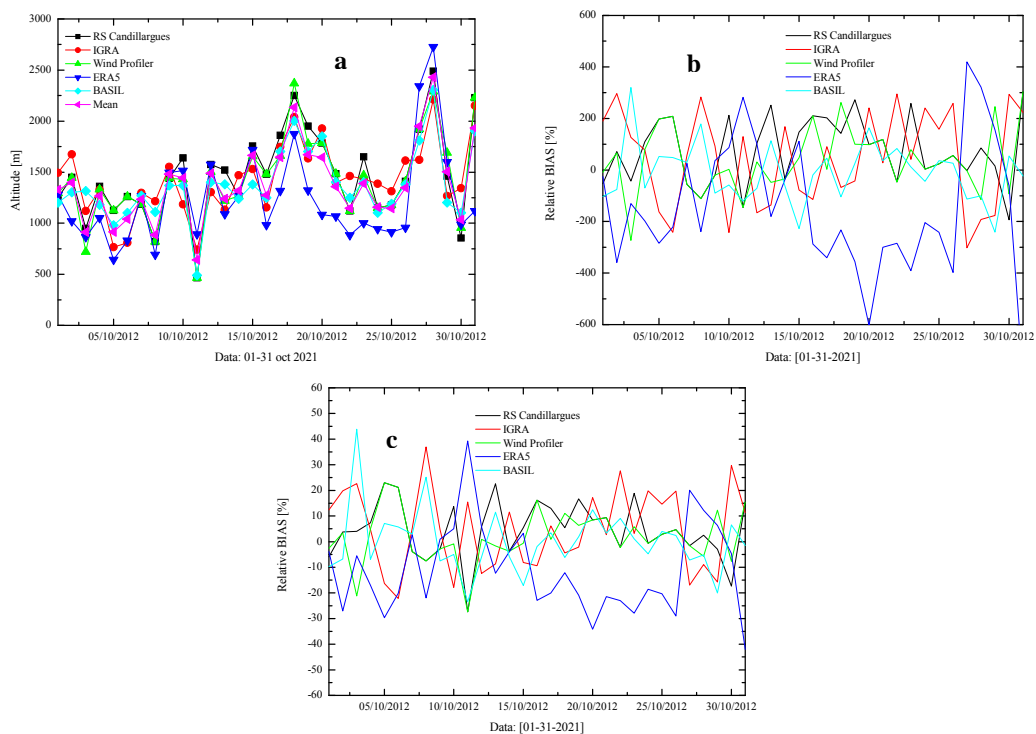
475 **Figure 2: (a)**, Time evolution of the ABLH over the time period 1-31 October 2012 as measured/modeled through the five approaches illustrated in section 2; Deviations, expressed both in meters (**b**) in percentage (**c**), between the ABLH estimate from the different approaches/sensors/models and the mean value obtained from the 5 considered approaches/sensors/models.

Date	Rs- Mean		IGRA-Mean		Wind Prof -Mean		ERA5 -Mean		Basil - Mean		Standard Deviation	
	Rel [%]	Abs [m]	Rel [%]	Abs [m]	Rel [%]	Abs [m]	Rel [%]	Abs [m]	Rel [%]	Abs [m]	Rel[%]	Abs[m]
01/10/20 12	-4,07034	-53,0381	14,60083	190,2544	-0,65793	-8,57312	-1,96502	-25,605	-7,90753	-103,038	8,610678	112,2004
02/10/20 12	5,189951	71,54134	21,51253	296,5413	4,827227	66,54134	-26,0556	-359,165	-5,47413	-75,4587	17,47774	240,9234
03/10/20 12	-4,37148	-43,4275	12,74099	126,5725	-27,5237	-273,428	-13,1152	-130,29	32,26934	320,5725	23,19651	230,4405
04/10/20 12	8,814189	110,163	6,21385	77,663	6,413876	80,163	-15,8542	-198,152	-5,58769	-69,837	10,48831	131,0868
05/10/20 12	21,2757	197,3616	-17,5325	-162,638	21,2757	197,3616	-30,6635	-284,446	5,644609	52,36156	23,37098	216,7982
06/10/20 12	19,75759	207,8747	-23,013	-242,125	19,75759	207,8747	-21,0525	-221,499	4,550281	47,87466	21,06083	221,5864
07/10/20 12	-4,4947	-55,7689	4,572255	56,73111	-4,4947	-55,7689	2,061266	25,57555	2,355887	29,23111	4,216315	52,31473
08/10/20 12	-11,9695	-111,495	30,43548	283,505	-11,9695	-111,495	-25,6598	-239,02	19,16327	178,505	23,65646	220,3587
09/10/20 12	-1,3505	-19,7134	6,356494	92,7866	-1,3505	-19,7134	2,490461	36,35359	-6,14596	-89,7134	4,69116	68,47749
10/10/20 12	14,8564	212,1301	-17,0092	-242,87	0,149182	2,130118	6,056541	86,47953	-4,05288	-57,8699	11,86546	169,4234
11/10/20 12	-23,8331	-145,502	21,21177	129,4983	-23,8331	-145,502	46,19266	282,007	-19,7381	-120,502	32,05204	195,6783
12/10/20 12	7,052154	103,7545	-11,2996	-166,246	2,124356	31,2545	6,965664	102,482	-4,84253	-71,2455	7,967093	117,2155
13/10/20 12	19,83377	251,5762	-10,716	-135,924	-3,81763	-48,4238	-14,2543	-180,805	8,954122	113,5762	14,19635	180,0699
14/10/20 12	-2,64637	-34,4545	12,90717	168,0455	-2,64637	-34,4545	-2,85587	-37,1821	-4,75858	-61,9545	7,269829	94,64986
15/10/20 12	9,153866	147,1779	-4,84022	-77,8221	2,934273	47,17789	6,921689	111,2884	-14,1696	-227,822	9,546184	153,4857
16/10/20 12	16,5895	210,5889	-9,01293	-114,411	16,5895	210,5889	-22,6369	-287,356	-1,52914	-19,4111	16,92944	214,9042
17/10/20 12	12,22715	202,647	5,439218	90,14704	0,159715	2,647041	-20,5803	-341,088	2,754214	45,64704	12,3516	204,7096
18/10/20 12	6,75762	142,4221	-3,20642	-67,5779	12,45136	262,4221	-11,0406	-232,688	-4,96199	-104,578	9,453813	199,2465
19/10/20 12	16,24552	272,516	-2,5326	-42,484	5,962264	100,016	-21,1963	-355,564	1,521089	25,51602	13,76113	230,8408
20/10/20 12	5,858497	98,78675	14,30939	241,2868	5,858497	98,78675	-35,7397	-602,647	9,713288	163,7868	20,27976	341,96
21/10/20 12	8,63276	118,009	2,048956	28,00904	8,63276	118,009	-21,9487	-300,036	2,634183	36,00904	12,66817	173,1727
22/10/20 12	-4,02414	-46,9601	25,32562	295,5399	-4,02414	-46,9601	-24,3932	-284,659	7,115913	83,03987	18,16206	211,944
23/10/20 12	18,59993	258,7681	2,9663	41,26811	5,661753	78,76811	-28,0739	-390,572	0,845877	11,76811	17,14401	238,513
24/10/20 12	0,288646	3,30988	21,00043	240,8099	0,288646	3,30988	-17,7676	-203,74	-3,81011	-43,6901	13,88695	159,2403
25/10/20 12	2,044014	23,58616	13,74333	158,5862	2,044014	23,58616	-20,9586	-241,845	3,127284	36,08616	12,71101	146,6741
26/10/20 12	4,157892	56,28597	19,11674	258,786	4,157892	56,28597	-29,3743	-397,644	1,941767	26,28597	17,79498	240,8931
27/10/20 12	-0,12207	-2,34659	-15,728	-302,347	-0,12207	-2,34659	21,81638	419,3863	-5,84424	-112,347	13,76144	264,5426
28/10/20 12	3,540505	85,14404	-7,99865	-192,356	-4,776	-114,856	13,38641	321,9238	-4,15226	-99,856	8,598851	206,79
29/10/20 12	1,112425	16,06271	-12,2192	-176,437	17,04109	246,0627	10,75179	155,2491	-16,6861	-240,937	14,44795	208,6193
30/10/20 12	-18,4436	-193,354	28,05785	294,1457	-8,90484	-93,3543	-5,92194	-62,0829	5,212524	54,64572	17,81113	186,7238
31/10/20 12	15,74554	303,3598	11,59323	223,3598	15,74554	303,3598	-41,8573	-806,439	-1,22701	-23,6402	24,41201	470,3316
Mean	4,5938	77,00018	4,485293	44,20317	1,869509	38,11196	-10,8491	-149,735	-0,09949	-9,58046	6,372381	89,22973

Table 1: Relative error in terms of [%] ABL (m) for each day in October month computed for the different instruments compared with the average value. The values represents the mean simple average in term of relative error.

Atmospheric
Measurement
Techniques
Discussions

485
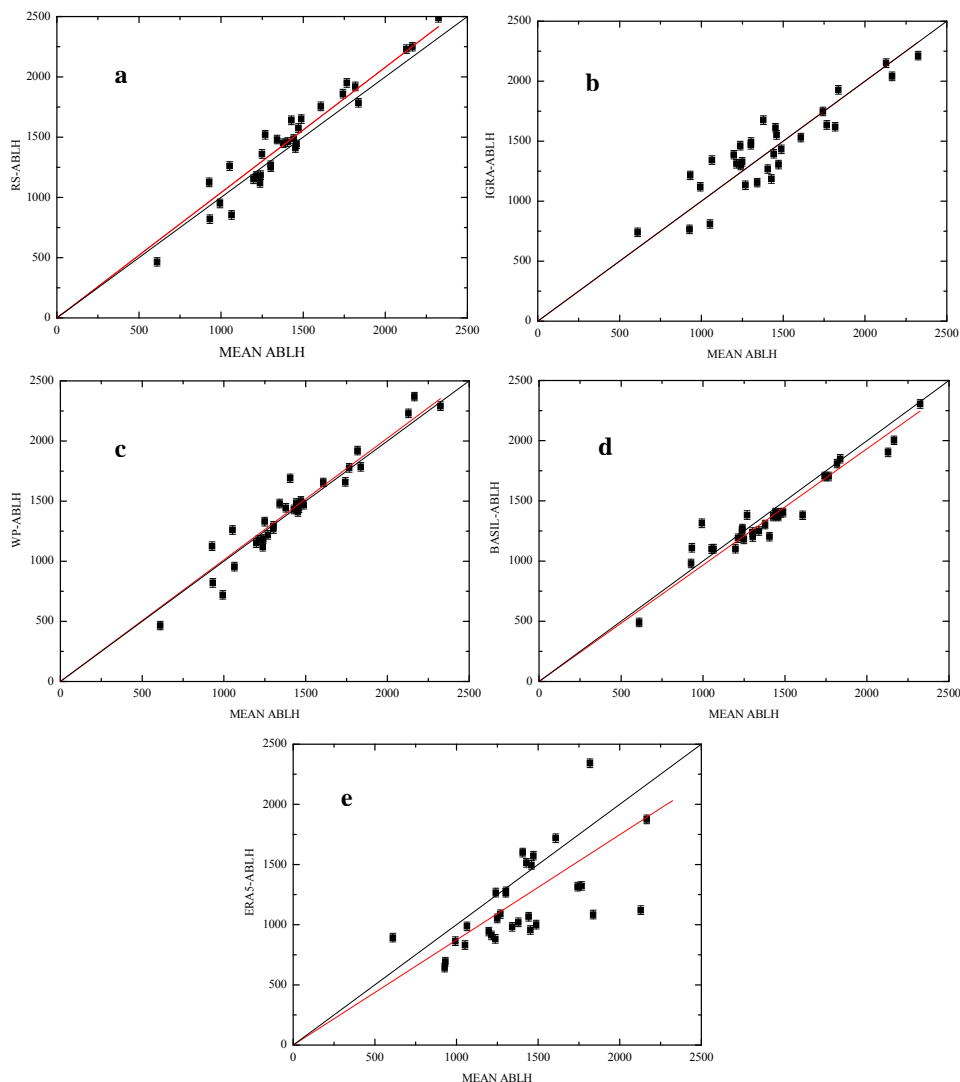
Figure 3: ABLH estimates obtained from the different sensor/model data expressed in terms of scatter plot, with the values of the mean reference ABLH obtained from the 5 different sensors/models in the X axes and the ABLH values from each single sensor/model in the Y axes. (**a**): Radiosondes in Candillargues, (**b**): IGRA radiosondes, (**c**): Wind profiler, (**d**): BASIL, (**e**): ERA5. The red lines

490   represent the linear fit applied to the data points, using a linear regression function with the form $Y = A \times X$. For the purpose of highlighting the deviation between the fitting lines and the 1:1 bisectors, these latter have also been reported.
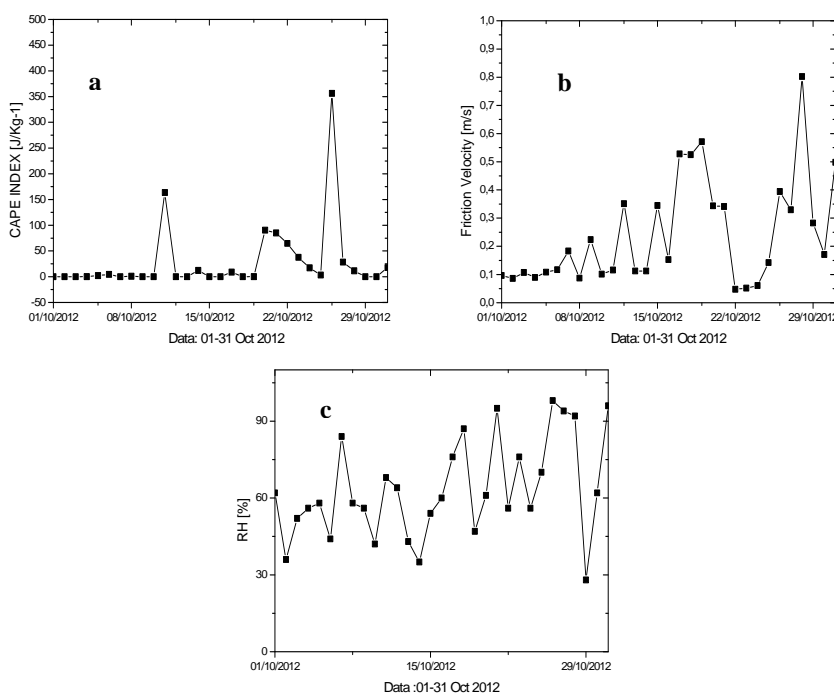
18

495

Summary-FIT Table [$Y = A \cdot X$]			
Comparison Methods	Slope		Correlation coefficient
Basil-vs	A	σ(A)	R^2
On-site RSs	1.04	0.01	0.94
IGRA-DB	1.00	0.01	0.81
WindProfiler	1.01	0.01	0.93
BASIL	0.97	0.01	0.91
ERA	0.87	0.01	0.52

500

505

Table 2: Results from the regression analysis, with values of the correlation coefficient R^2 and the regression line slope A, with its standard deviation σ(A).

510

Figure 4: ERA5 atmospheric reanalysis for CAPE (panel a), friction velocity (panel b) and relative humidity (panel c).

19

515

Correlation Index	Era5-ABL	Mean-ABL
CAPE	0.49	0.52
Friction	0.71	0.75
RH	0.34	0.42

520

Table 3: (upper line) Correlation coefficients of ERA5 and mean ABLH estimates versus the corresponding friction velocity values; (mid line) Correlation coefficients of ERA5 and mean ABLH estimates versus the corresponding CAPE gradient values; (lower line) Correlation coefficients of ERA5 and mean ABLH estimates versus the corresponding relative humidity (RH).

525
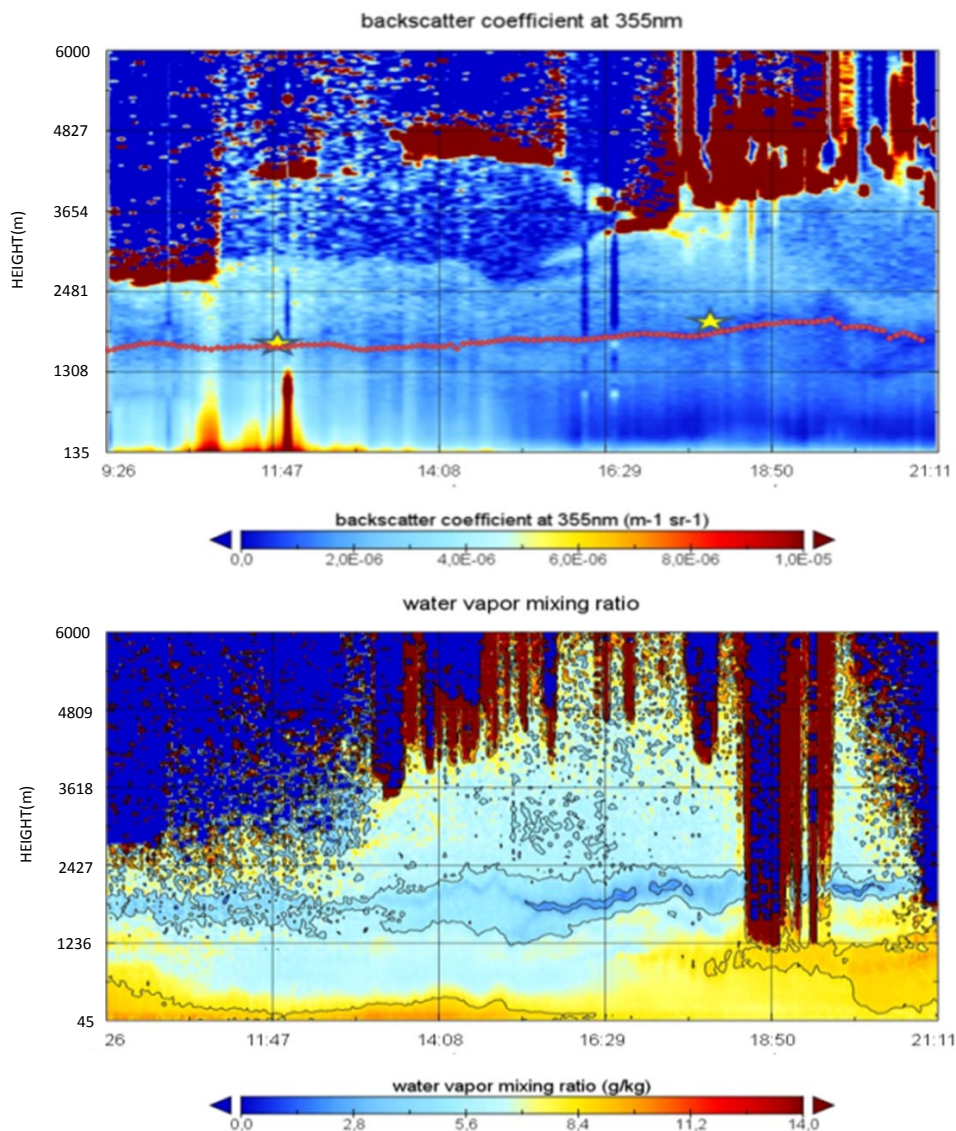
Figure 5: Time-height cross-section of the particle backscattering coefficient at 355nm, $\beta_{355}(z)$, (left panel) and water vapour mixing ratio (right panel) over the time interval 09:26-21:11 UTC on 18 October 2012 as measured by BASIL. The map is conceived as a succession of profiles of $RCS(z)$. Red dots in panel a identify the ABLH as determined from BASIL measurements based on the application of the method illustrated in the section 2.2, while yellow stars identify the ABLH as determined from the radiosonde data based on the application of the temperature gradient method.